applied sciences

MDPI

Article

Effect of Ti-B Grain Refiners on Wear and Corrosion of the A332 Alloy with Sr Modification

Bruno E. Arendarchuck [1], Andre R. Mayer [2], Willian R. de Oliveira [1], Anderson G. M. Pukasiewicz [1], Luciano A. Lourençato [1], Hipolito D. C. Fals [1] and Eduardo Martínez-Cámara [3,*]

[1] Department of Mechanical Engineering, Federal University of Technology—Paraná, Ponta Grossa 84017-220, Brazil
[2] Department of Mechanical, Industrial and Aerospace Engineering, Concordia University Montreal, Montreal, QC H3G 1M8, Canada
[3] Department of Mechanical Engineering, University of La Rioja, 26004 Logroño, Spain
* Correspondence: eduardo.martinezc@unirioja.es; Tel.: +34-941-299-533

Abstract: Grain refiners play a critical role in changing characteristics and properties of casting aluminum alloys. The Al-Si alloy (A332) is one of the most popular hypoeutectic alloys with a large range of industrial applications. It has a varied phase and morphology; however, it features problems with acicular-shaped eutectic phase, and generally exhibits dendritic cast grain type. To change this situation, the Sr element acts as a modifier of eutectic, which, along with a grain refiner may increase mechanical properties. In this work, two different grain refiners (Al5Ti1B, Al5Ti2B) were applied to the A332 alloy modified with Sr, and analyzed in relation to grain size, hardness, corrosion resistance, and wear behavior. Corrosion tests in 3.5 wt.% NaCl solution, nanoindentations, and Heyn's method to analyze grain size and microhardness as optical and SEM images were made to examine the changes caused by grain refiners. A reduction in grain size was achieved, and the influence in size and hardness of the β-Fe phase was verified in the wear and corrosion analyses.

Keywords: Al-Si cast alloys; AlTiB grain refiners; iron-containing intermetallics; strontium modifier; microstructure; nanoindentation; corrosion rate; hardness; wear resistance

Citation: Arendarchuck, B.E.; Mayer, A.R.; de Oliveira, W.R.; Pukasiewicz, A.G.M.; Lourençato, L.A.; Fals, H.D.C.; Martínez-Cámara, E. Effect of Ti-B Grain Refiners on Wear and Corrosion of the A332 Alloy with Sr Modification. *Appl. Sci.* **2023**, *13*, 430. https://doi.org/10.3390/app13010430

Academic Editors: Gabriele Arcidiacono, Paolo Citti and Alessandro Giorgetti

Received: 25 November 2022
Revised: 13 December 2022
Accepted: 26 December 2022
Published: 29 December 2022

1. Introduction

The A332 aluminum alloy is a hypoeutectic Al-Si–Mg, which has a wide range of applications, such as common industry products in the automotive and aerospace industries, mainly due to its suitable casting properties and excellent weldability [1]. However, as-cast Al-Si alloys are composed of coarse primary face centered cubic aluminum phase dendrites and acicular-shaped eutectic phase, which lowers the mechanical properties and limits its industrial application potential [2]. Some methods can be used to solve this issue, mainly by adding elements such as Sr and Na used to modify the eutectic phase [3]. Adding Sr to molten aluminum has a metamorphic effect, which can effectively refine the eutectic phase and primary Si in the alloy, improving the mechanical properties of the alloy [4]. The effects of adding Al5Ti1B, Al3B, and Al10Sr in LM6 Al-Si alloy were analyzed by Prema et al. [5]. The LM6 alloy was cast, and each master alloy was added individually and then tested for mechanical properties. The results show a grain size reduction and wear resistance increase with any master alloy.

Moreover, the failure and mechanical properties of Al-Si casting alloys are strongly dependent on macro and microstructural features, such as size, morphology, and the distribution of primary aluminum dendrites, eutectic phase, and Fe intermetallic compounds [6]. In this sense, the Fe element, which is an impurity, is necessarily present in commercial Al alloys, as it reduces the die-casting surface flaws and increases the high temperature properties, with a better thermal stability of the alloy. However, Fe affects the mechanical

properties, mainly caused by the precipitation of brittle intermetallic phase, Al_5FeSi, that appears in morphologies such as needles or plates in the microstructure [7].

To reverse this issue, some methods have been used. Grain refiners (GR) are amongst the most efficient ones. Many advantages can be obtained from using grain refiners, such as better mechanical properties, reduced hot cracking susceptibility and better corrosion and wear resistance. The influence of grain size ($d > 1$ μm) on yield strength (σ_y) of metals follows the Hall–Petch relationship showed in Equation (1).

$$\sigma_y = \sigma_o + kd^{-0.5} \quad (1)$$

where (d) is the grain diameter, (σ_o) is the frictional stress, and (k) is a constant, generally understood as an influence of grain boundaries on strength [8].

There are several means to prepare fine-grained materials employing the most commonly used methods, i.e., friction stir processing, electrodeposition, equal-channel angular pressing, severe plastic deformation and chemical grain refinement, one of the most used in aluminum alloys [9]. The main approach to chemical grain refinement is the inoculation in the molten material with a nucleating agent. In the grain refinement of aluminum alloys, commercial ternary Al-Ti-B master alloys are added to suppress the growth of columnar grains and promote the formation of equiaxed fine-grain structures throughout the casting. The most common and commercially available ones are Al-Ti-B master alloys. For a better understanding of the grain refinement mechanism, several theories have been proposed. A substantial number of researches demonstrated that TiB_2 particles inoculated into Al melt via Al-Ti-B master alloys enhanced heterogeneous nucleation of primary aluminum grains. In conjunction with solute Ti atoms, this promoted the nucleation efficiency of TiB_2 to reach a complete wetting of TiB_2 particles with molten aluminum.

Other particles that play an important role in the result are the soluble Al_3Ti particles dispersed in the aluminum matrix. The former act as heterogeneous nucleation sites while Al_3Ti particles readily dissolve in the molten material and provide solute Ti that partitions between the solid and liquid phases during solidification and, in this way, slows the growth process [10]. The ratio between Ti/B in master alloys and the way of processing conditions lead to a different morphology of the Al_3Ti particles, which may have resulted from different growth mechanisms [11].

The effectiveness and mechanisms of grain refiners might be altered by introducing different methods and temperatures. Gyarmati et al. [12] evaluated the influence of melting temperatures of 800 °C and 650 °C in the Al7Si refined with Al10Ti. Image analyses of optical micrographs led to the characterization of the grain refiner particles in the Al10Ti master alloy and the sediment layers formed during the experiments. When the master alloy was added at a constant 690 °C, undissolved blocky particles settled at the bottom. In this case, grain refinement was not accomplished. In the meantime, an effective grain refinement when the grain refiner was first dissolved at 800 °C and re-precipitated at 690 °C, showing the importance of using appropriate temperatures. Similar results were observed in other works. Modifications and grain refiners were applied to achieve desired properties. Nevertheless, adding grain refiners may produce undesirable effects. Limmaneevichitr and Eidhed [13] studied the impact of the Al-Ti-B grain refiner on the fatigue mechanism of the A332 aluminum alloy. The results show a different concentration of Ti and B through the sample, which affects the properties. The difference in density of both particles (Al_3Ti and TiB_2) is the primary factor affecting the fading mechanism. Thus, carefully inserting materials in the molten material is essential to have an effective action in the aluminum alloy.

Other studies have suggested that the grain refiner addition promotes changes in microstructural features and directly relates to mechanical properties. Choudhary et al. [14] evaluated the variation of wt% of Al5Ti1B grain refiner on the microstructural features of Al7Si alloy. X-ray diffraction (XRD), scanning electron microscope (SEM), high resolution transmission electron microscope (HRTEM), and thermodynamic analysis were used. The morphology of primary aluminum grain changes from a coarse dendritic structure to a

fine equiaxed grain. The eutectic phase was also refined, and the presence of an iron-based intermetallic was observed. From mechanical properties, the grain refiner addition took an increase in hardness and yield strength. The refined alloy's fracture mechanism changed from brittle to ductile fracture. Albeit elongation decreased when the percentage of Ti increased by more than 0.1 wt.%.

The combined action of Al5Ti1B grain refiner with Al10Sr modifier may show better results than only using the grain refiner. Tunçay [15] used grain refining (Al5Ti1B) and modifier (Al10Sr) to determine the effect of modification and grain refining on the microstructure and mechanical properties of A356 aluminum alloy. It was concluded that the sharp-edged morphology of the eutectic phase tended to be spherical with Sr addition. Furthermore, the porosity was reduced, increasing Al5Ti1B up to 1.5 wt.%. In addition, the presence of Al5Ti1B promotes an increased average ultimate tensile strength, and the percentage of elongation increases as well.

The grain refiner's efficiency was also tested with distinct Al-Si alloys and molds. Çolak and Arslan [16] evaluate the effects of Al5Ti1B grain refiner and Al10Sr modifier additives on friction and wear properties on A380 and A357 alloys, using the pin-disk test. Their results show that grain refiner and modifier additives decrease the friction coefficient and increase the wear resistance, headlining the need for studying several combinations of the alloy, grain refiner, and modifier.

Sumalatha et al. [17] researched the wear behavior of cast Al16Si alloy with five different compositions of Al5Ti1B grain refiner, Al5Sr modifier, and graphene. An evident transformation of eutectic silicon to rounded particles can be observed through the microstructural analysis. In the mechanical properties, the alloy reinforced with graphene shows higher hardness values, followed by the condition with grain refiner and Sr. A similar effect was observed in the wear tests, highlighting the positive impact of combining grain refiner and Sr modifier. Although some studies analyze the effect of grain refining in the Al-Si alloys, few papers study the relationship between corrosion, wear, mechanical properties, and grain refinement. Ralston and Birbilis [18] suggest that an increase or decrease in corrosion resistance of the alloy with grain refinement depends on the ability of the environment to make the alloy passivated. El-Aziz et al. [19] mentioned that the addition of a GR alloy did not reveal any marked improvements in the corrosion properties of Al-Mg–Si alloy.

Revision and extensive literature review of the works of Guan and Tie [20] about grain refining, and by Wang et al. [9] about grain refinement and corrosion in metals, shows several methods for grain refining and their results applied to cast aluminum alloys. Nevertheless, there is a lack of studies on the relationship among corrosion, wear, and mechanical alterations in the combination of specific AlTiB master alloys and Sr modifiers in the hypoeutectic Al-Si alloys.

This research is aimed at studying the effect of individual addition of two different grain refiners, Al5Ti1B and Al5Ti2B, in an A332 hypoeutectic aluminum alloy modified with Al10Sr in ball-on-disk wear, corrosion, mechanical properties, and microstructural changes.

2. Materials and Methods

The A332 commercial aluminum base alloy, with chemical composition provided by the supplier, as shown in Table 1, was cast in a 35 kW commercial GRION induction furnace at a temperature of 750 °C. Four refinement conditions were used, as shown in Table 2. Two master alloys were utilized to refine the A332, Al5Ti2B, and Al5Ti1B, one without refiner. Samples without refiner added (as-cast), samples refined with 93 wt.% Al, 5 wt.% Ti, 2 wt.% B (Al5Ti2B), and samples with addition of 94 wt.% Al, 5 wt.% T, 1 wt.% B (Al5Ti1B). For all the conditions, 200 ppm of Sr was used as modifier with the alloy 90 wt.% Al, 10 wt.% Sr (Al10Sr).

Table 1. Chemical composition provided by supplier of A332 alloy (wt.%).

Si	Fe	Cu	Mn	Mg	Zn	Ni	Cr	Pb	Ti	Sr
8.734	0.895	2.757	0.183	0.252	0.993	0.121	0.025	0.063	0.059	0.001

Table 2. Alloy compositions prepared as a function of grain refiner (wt.%).

Castings Samples	Alloy A332	Refiners		Modifier Sr
		Ti	B	
As-cast	99.98	0	0	0.02
Al5Ti2B	92.98	5	2	0.02
Al5Ti1B	93.98	5	1	0.02

Pouring was made, using cylindrical steel molds with a diameter of 31 mm and a length of 250 mm, prepared with a release agent and preheated up to 200 °C for 10 min before casting.

2.1. Metallographic Characterization and Mechanical Testing

The cylindrical cast specimens were machined up to 30 mm in diameter and then sectioned, subsequently roughened, and finally polished with 0.04 µm colloidal silica in a Vibromet2 vibratory polisher.

Optical microscopy (OM) analyses were performed on a ZEISS Axio Imager A2 microscope with magnifications of 100× and 200×. SEM images and energy dispersive spectroscopy (EDS) analyses were also performed using a Vega Tescan scanning electron microscope operating at 20 kV, using secondary electron (SE) and back scattered (BSE) images at magnifications of 200× and 1000×. No etching was used to obtain the images.

To determine the Vickers hardness, measurements with 100 g with 15 s were performed. Ten measurements were made per sample, obtaining the average of these values in the microhardness tester (HMV-G20ST SHIMADZU).

Furthermore, nanoindentation analyses were conducted in two steps. Firstly, hardness and elastic modules of the phases in the microstructure were analyzed using nanoindentation instrumented by Quasi Continuous Stiffness Measurement (QCSM), with an average of 10 indentations, carefully positioned in the center of each grain of the corresponding phase with a maximum load of 30 mN. Secondly, an instrumented nanoindentation analysis was made with a 20 × 20 matrix, using the fast H-E method at full load of 30 mN. The tests were performed in a UNAT Asmec (Dresden, Germany) equipment using a Berkovich type pyramidal diamond tip at UEPG Multi-User Laboratory—C-LABMU (Ponta Grossa, PR, Brazil).

Grain size determination was performed on optical microscopy images, using the Heyn Intercept method governed by the ASTM E112 [21]. Four images were analyzed per sample, with one segment horizontal, one vertical and one straight at 45°, these had a length of 3 times the scale; 15 sets were allocated per image. The volume fraction, thickness, and length of the (Al_5FeSi) were measured by quantitative metallography using MEV images in a computer-assisted image analysis system open software ImageJ.

The technique of optical emission spectrometry in a SHIMADZU PDA 7000 equipment was used for the analysis of the chemical composition of the samples.

2.2. Ball-on-Disk Wear Testing

The test was made with the High Temperature Tribometer equipment (CSM Instruments, Buchs, Switzerland), Figure 1. The 29 mm circular samples were cut in a thickness of 6 mm, and then followed by standard metallographic preparation to obtain a mirror finish.

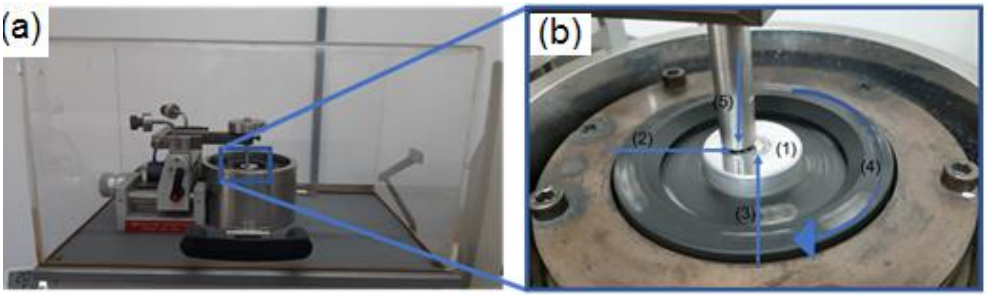

Figure 1. (**a**) equipment for ball-on-disk testing; (**b**) detailed scheme of testing (1) sample, (2) ball, (3) wear path on sample (4) rotation sense of sample and (5) load.

The tests were performed without lubrication, at room temperature. The parameters of the ball-on-disk testing are shown in Table 3. The friction coefficient (μ) between the Al_2O_3 spheres and A332 samples was measured for each cycle and this value was plotted. The characterization of the worn tracks was performed through SEM images and non-contact optical profilometer (OP).

Table 3. Parameters of ball on disk testing.

Diameter of Path (mm)	Ball Diameter (mm)	Sliding Speed (m/s)	Load (N)	Number of Cycles
8	6	0.1	3	15,000

The volume loss of the wear track was obtained using OP, assuming no significant wear of the sphere used in the test, due its high hardness in relation to the surface tested. The optical profilometer obtained images of the worn tracks after the ball-on-disk testing. The volume loss was obtained from the 3D view of the complete worn tracks in all the samples from the equipment software calculation, using the surrounding tooth surface as the reference plane. The volume of a hole was measured and used as a value of volumetric loss. The relative wear resistance (Ψ_h) was calculated from Equation (2) [22], i.e., lower values represents lower wear resistance.

$$\Psi_h = \frac{W_{hE}}{W_{hPV}} \quad (2)$$

where W_{hPV} is volumetric loss standard (mm^3), and W_{hE} is volumetric loss of reference sample (mm^3).

Furthermore, the line profiles were extracted from the surface to show a cross-sectional view of the wear track. The equipment used was an optical profilometer 3D CCI Lite from Tyler Hobson, with an optical lens of 10×.

2.3. Corrosion Analysis

Corrosion analyses were made with Autolab Potentiostat PGSTAT M204, FRA32M equipment (Ultrecht, Netherlands), according to ASTM G59-97 [23], G102-89 [24], and G5-14 [25] standards. In order to induce pitting corrosion a 3.5 wt.% NaCl solution at 25 °C was used as environment. The samples were polished using colloidal silica to achieve a mirror finish. A calomel (3.0 M KCl) reference electrode and platinum counter electrode were used for measurements. The samples were prepared in a cylindrical shape with 17 mm of diameter and 4 mm height. The samples were placed inside of support, exposing 1 cm^2 of its area. Open circuit potential (E_{ocp}) was measured for 55 min and the chemical reaction was considered stabilized after that, according to ASTM G5 [25]. A resolution of 1 $mV{\cdot}s^{-1}$ was used both for micro and macro polarizations. A potential range of $E_{ocp} \pm 20$ mV was used for acquiring micro-polarization curves, used to calculate polarization resistance (Rp). A potential range of E_{ocp} from −1 V up to +5 V was used for macro-polarization. A wide

range of potential was used for Tafel curves in order to generate pitting corrosion. Anodic (b_a) and Cathodic (b_C) were measured from Tafel slopes. Likewise, corrosion potential and current density were measured at the intersection of the slopes. The corrosion rate CR (mm/year) was calculated in accordance to Equation (3) ASTM G59—97 [23], in which EW is the equivalent weight of the corroding species (g), i_{corr} is the current density ($\mu A/cm^2$) and ρ is the density of the corroding material (g/cm^3).

$$CR = 3.27 \times 10^{-3} \frac{i_{corr} EW}{\rho} \quad (3)$$

3. Results

3.1. Microstructure Characterization

To begin the analysis, Figure 2 shows the optical images from the A332 alloy in as-cast condition without grain refiner(a), and using Al5Ti2B (b) and Al5Ti1B refiners (c). The as-cast condition shows that the morphology of elongated arms of dendrites, while the other samples have more equiaxed grains. This modification of the shape and size of the grains is the result of the effect of increasing the formation of solidification nuclei when the different refining alloys, with Ti and B (AlTiB) were added. Regardless of the type of refiner, all the samples showed a primary aluminum phase, the eutectic phase, refined by the Sr modifying effect [26], and the intermetallic Fe and Cu phases, with different morphology.

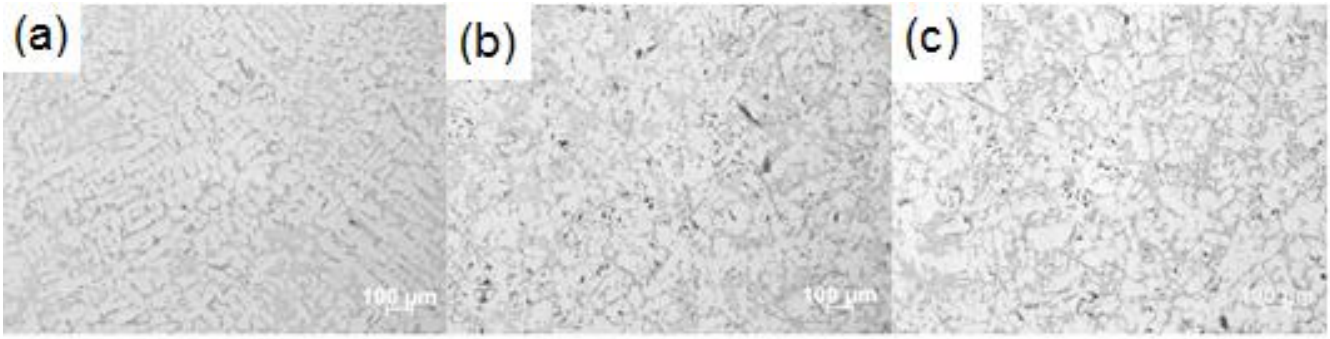

Figure 2. Optical micrographs showing the microstructure from (**a**) A332 alloy in as-cast condition without grain refiner; (**b**) with grain refiner Al5Ti2B; (**c**) with grain refiner Al5Ti1B.

Pore formation was observed in all samples, though it was not significant. However, the unrefined condition was found to have a lower amount of pores, this is probably related to the greater amount of hydrogen induced during the refinement process, as evidenced by El-Sayed [27].

To confirm the type of the phases, EDS with line scan technique was used to identify the chemical elements, in each relevant region. Figures 3 and 4 show an (a) SEM image from an SE, and (b) respective EDS line scan from the marked square in the images (a).

The SEM image in Figure 3 shows the microstructure of samples obtained without the use of a grain refiner, with visible different phase morphologies. Figure 3b shows, as a result of the line scan chemical analysis, that the elements Fe, Mn, and Si present high peaks, in the phases in the form of grouped polyhedral, confirming the phase called "Chinese-Script" $Al_{15}(FeMn)_3Si_2$. In addition, on the right side of the "Chinese-Script" phase, another Fe-rich needle-shape phase Al_5FeSi is observed and proved by the Fe peaks in the EDS [28].

Figure 4a shows a secondary electron image from the sample with Al5Ti1B grain refiner. It also shows a respective EDS line scan (b) from the highlighted square in (a) to identify the chemical elements peaks. In this sense, the analysis confirmed that the $Al_{15}(FeMn)_3Si_2$ phase was only formed in the samples without the addition of grain refiners. Most likely, the influence of grain refiners, low concentration of Mn and Cr in the composition of the

332 alloy, the use of the Sr modification, and the high solidification rate inhibit formation of the $Al_{15}(FeMn)_3Si_2$ phase [29].

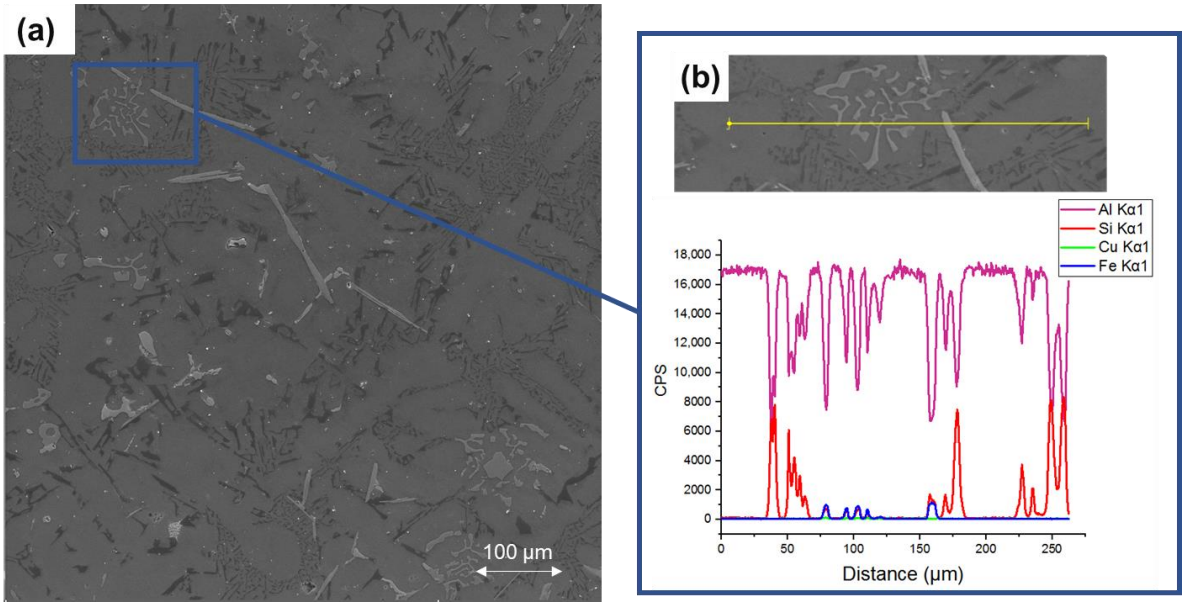

Figure 3. (**a**) A332 Secondary electron image of Chinese-script phase with; (**b**) corresponding EDS line scan showing the elements of this phase 200× present in the sample without grain refiner.

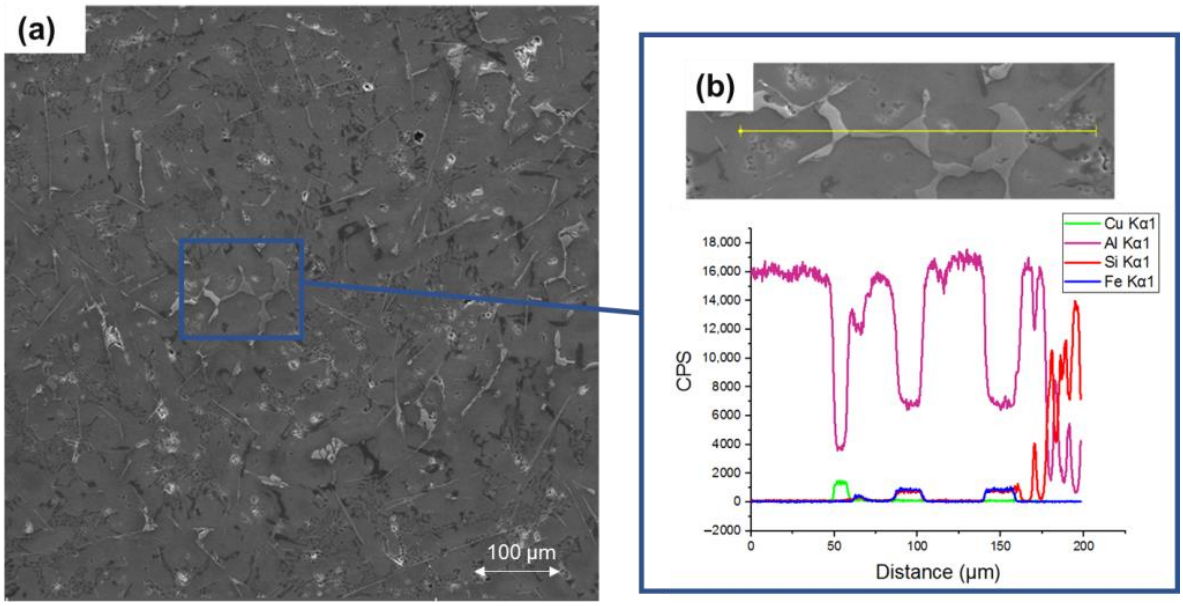

Figure 4. (**a**) Secondary electron image A332 with Al5Ti1B; (**b**) corresponding EDS line scan showing the elements peaks of Al_2Cu phase 200×.

Figure 4 also shows in a light grey form the Cu peak and in a dark grey form the Fe peaks, as well as other regions with Si peaks. The Cu peaks show the presence of the Al_2Cu phase, a common structure present in the Al-Si-Cu alloys [30].

In Figure 5, the SEM images show the all-samples cross-sections. These images are presented in order to allow the analysis of the influence of the type of refining on the formation of needles-like Al_5FeSi intermetallic phases. A general observation shows that in Figure 5, the needles Al_5FeSi phase was formed mainly in the eutectic zone, although some were also observed inside the primary aluminum phase.

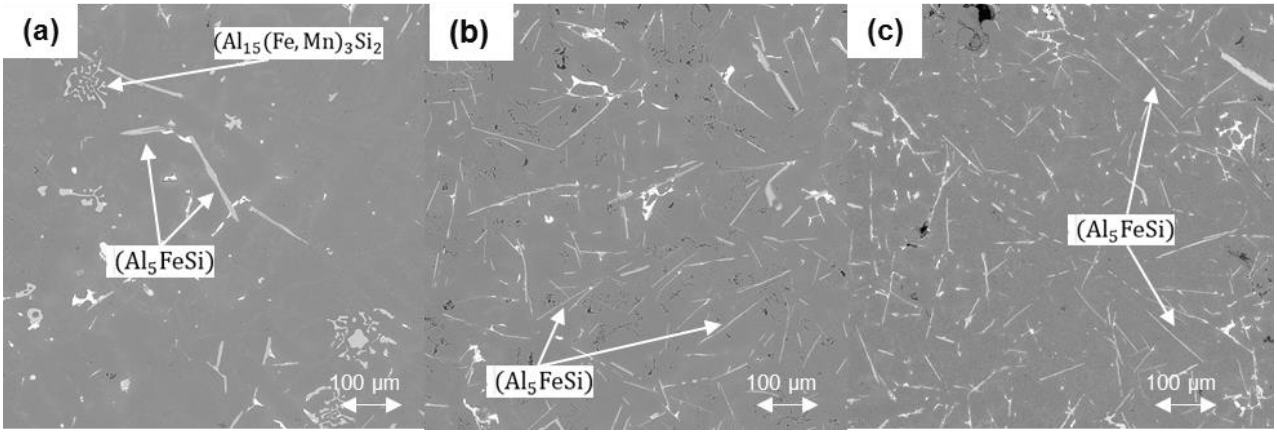

Figure 5. Cross section of SEM images (**a**) cast condition without grain refiner; (**b**) grain refiner Al5Ti2B; (**c**) grain refiner Al5Ti1B—200×.

The volume fraction, thickness, and length (µm) of the Al_5FeSi was measured by the quantitative metallography using MEV. It was found that the grain refining process influenced the amount of Al_5FeSi phase in the alloy. In this sense, despite the lack of significant differences, there is a slight tendency to increase the volumetric fraction of the Al_5FeSi phase, which ranged from 3.6 ± 1.45% in the cast alloy without refiner to 4.2 ± 0.74% in the refined alloy with Al5Ti1B. However, there were changes in the morphology of this phase, varying the thickness and length, as shown in Figure 6.

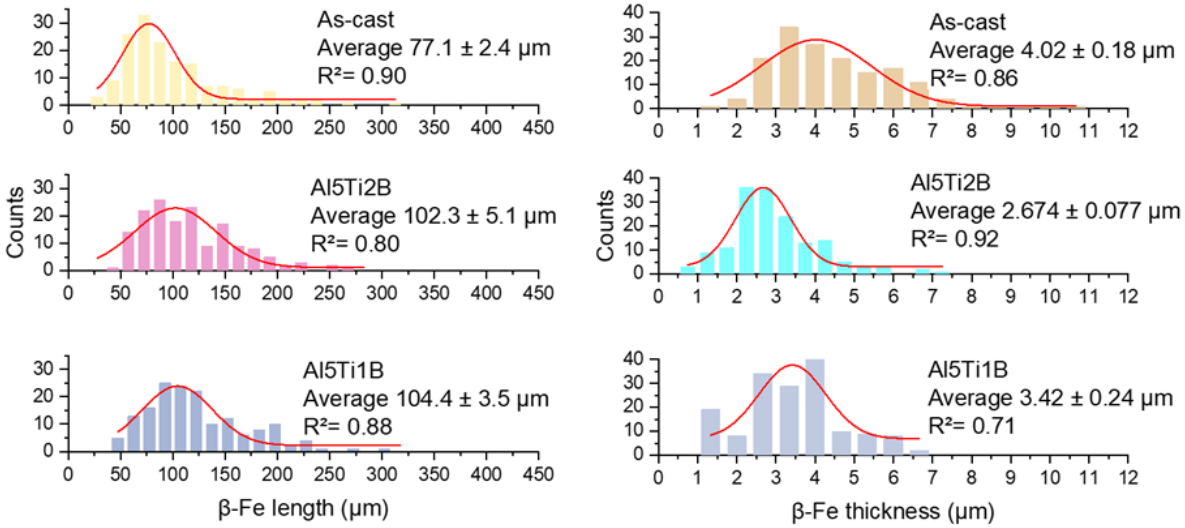

Figure 6. Length and thickness of the intermetallic beta iron (Al_5FeSi).

Figure 6 shows the difference of the average values of the thickness and length of the Al_5FeSi intermetallic phase, depending on the type of refiner used. An increase in the length of the needles of the intermetallic phase can be verified, however, thickness decreased when the different refiners were used.

The length of the Al_5FeSi phase increased from 77.1 ± 2.4 µm in the alloy in the as-cast without the refiner condition to 104.4 ± 3.5 µm when the Al5Ti1B refiner was used. However, no significant differences in length were observed when the type of refiner was modified, with more B (2 wt.%) in the composition. In addition, the thickness of the Al_5FeSi phase also proved influential, decreasing the thickness from 4.02 ± 0.18 µm to 2.67 ± 0.07 µm, with the addition of the Al5Ti2B refining type.

3.2. Primary Aluminum Phase Grain Size and Hardness

The alloy obtained without a refiner, as expected, showed a dendritic structure with a larger size of the primary aluminum phase. In general, the refiner alloys of the Al-Ti-B family increased the formation of solidification nuclei and thus showed a clear trend of microstructure refinement as verified through the analysis in Figure 7. However, there is a high standard deviation of the mean values of grain size. In this sense, it is important to explain that a factor that affects the increase in the standard deviation is the difficulty of delimiting the contours of the primary aluminum phase, where the eutectic phase is located in the contours of the primary aluminum phase, acquiring a fine and fibrous morphology due to the Sr modifying effect.

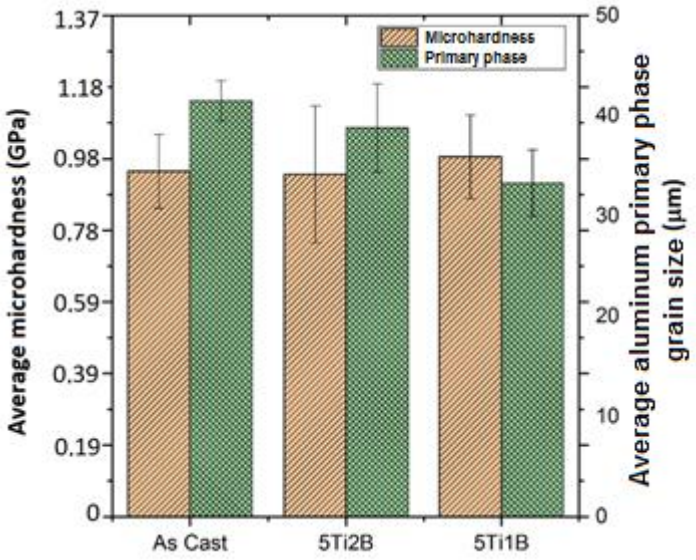

Figure 7. Variation of the primary phase grain size (μm) and microhardness (GPa) in the A332 alloy with different grain refiners.

Nevertheless, a greater grain size reduction was observed in the alloys refined with Al5Ti1, although, the standard deviation remained within the same values as in the previous conditions.

In general, when analyzing the microhardness of the alloys, it can be observed though that the Hall–Petch relationship is fulfilled, that is, the hardness increased with the decrease in grain size. The highest average values of microhardness were obtained in samples refined withAl5Ti2B, which showed the highest microstructural refinement. Under all conditions, there is great variation in the values of the standard deviation of microhardness, because of the different phases that make up this aluminum alloy.

3.3. Nanoindentation Analyses

It becomes clear that different phases can modify both hardness and the average material's modulus of elasticity. Most works only use an average value that is measured using microindentation equipment. The measurement made in instrumented nanoindentation allows the analysis of both the hardness and modulus of elasticity separately and with higher precision.

Figure 8 shows the results of instrumented nanoindentation analysis performed using the QCSM method, in as-cast samples without a refiner. It was conducted from an average of 10 indentations, carefully positioned in the center of each grain of the corresponding phase with a maximum load of 30 mN. Grains with at least 20 μm were also chosen to set the nanoindentations, except for the aluminum matrix, which had a larger area, where the positioning was relatively easier. The relatively low load was determined through initial

testing so that hardness results had a minimal influence from the aluminum matrix or other phases.

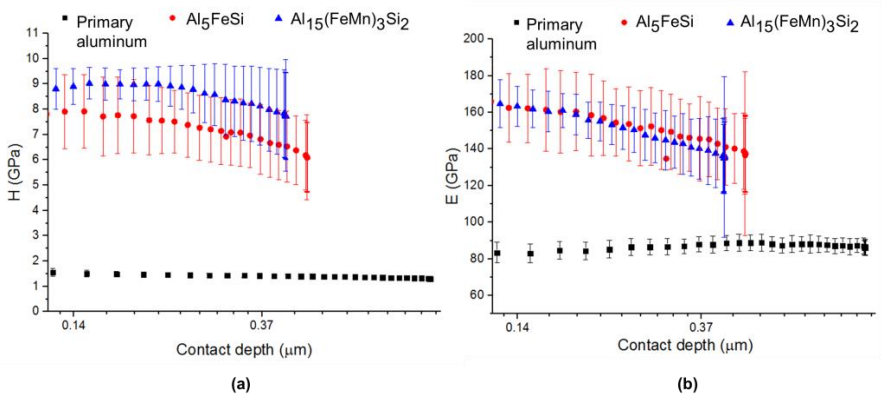

Figure 8. Instrumented nanoindentation analysis performed using the QCSM method, in A332 as-cast samples. Average of 10 indentations made with an indentation positioned at the center of the phase resulting in (**a**) hardness; (**b**) modulus of elasticity.

The graphs in Figure 8 show that the highest hardness values (a) (7.8 GPa in the Al_5FeSi phase and 8.9 GPa in the $Al_{15}(FeMn)_3Si_2$ phase) and the modulus of elasticity (b) (161 GPa in the Al_5FeSi phase and 163 GPa in the $Al_{15}(FeMn)_3Si_2$ phase), appear in the Fe intermetallic phases. These phases are present, as proven, in the A332 alloy in a molten state without the use of refinement. This also demonstrated that the values of hardness and modulus decrease with the increment of indentation penetration, which may be related to the effect of the primary aluminum matrix.

Figure 9 shows an instrumented nanoindentation map, made at full load of 30 mN, with SEM-SE images (c) e SEM-BSE (d) and EDS maps of the elements Fe (e) and Si (f). In general, as shown, both hardness and elasticity modulus are higher in intermetallic rich Fe phases ($Al_{15}(FeMn)_3Si_2$; Al_5FeSi). This fact can be observed in the small nanoindentation formations in the Fe-phases, showed in the Figure 9c,d.

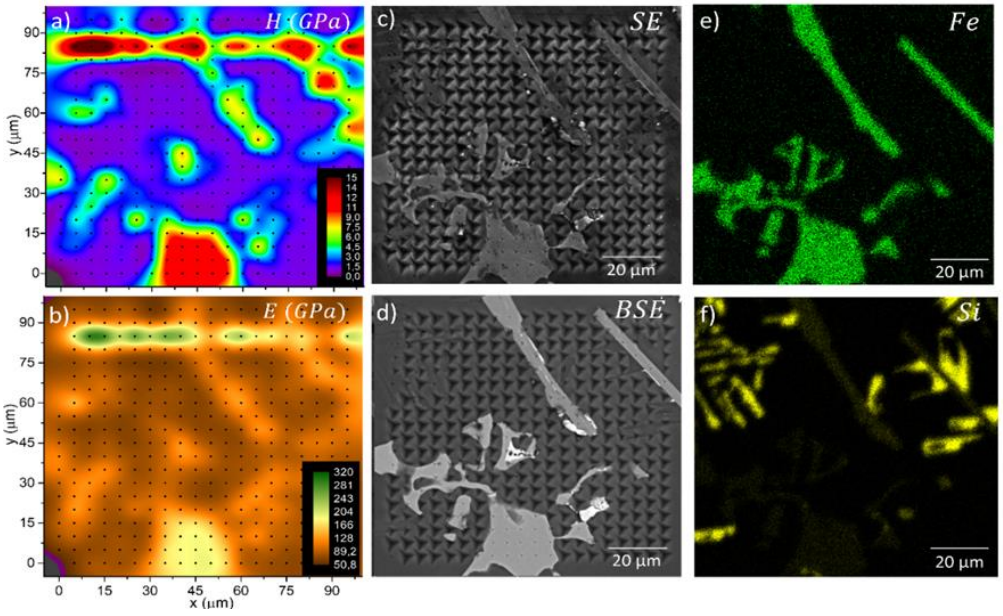

Figure 9. Instrumented nanoindentation analysis with a 20 × 20 matrix using the fast H-E method. (**a**) Hardness; (**b**) elastic modulus maps of a region with different types of phases, where each point represents an identification; (**c**,**d**) SEM-SE and SEM-BSE images; (**e**,**f**) EDS-Map of Fe and Si.

3.4. Effect of Grain Refiner Addition on Wear Behavior

Figure 10a–c shows the sliding wear track, after the ball-on-disk test using the Al_2O_3 sphere and load 3 N. Figure 10d–f shows the SEM and 3D profilometer images of the wear track after the ball-on-disk test. A plastic deformation can be seen in all conditions and the tendency of deep and shallow regions in circular-type formations.

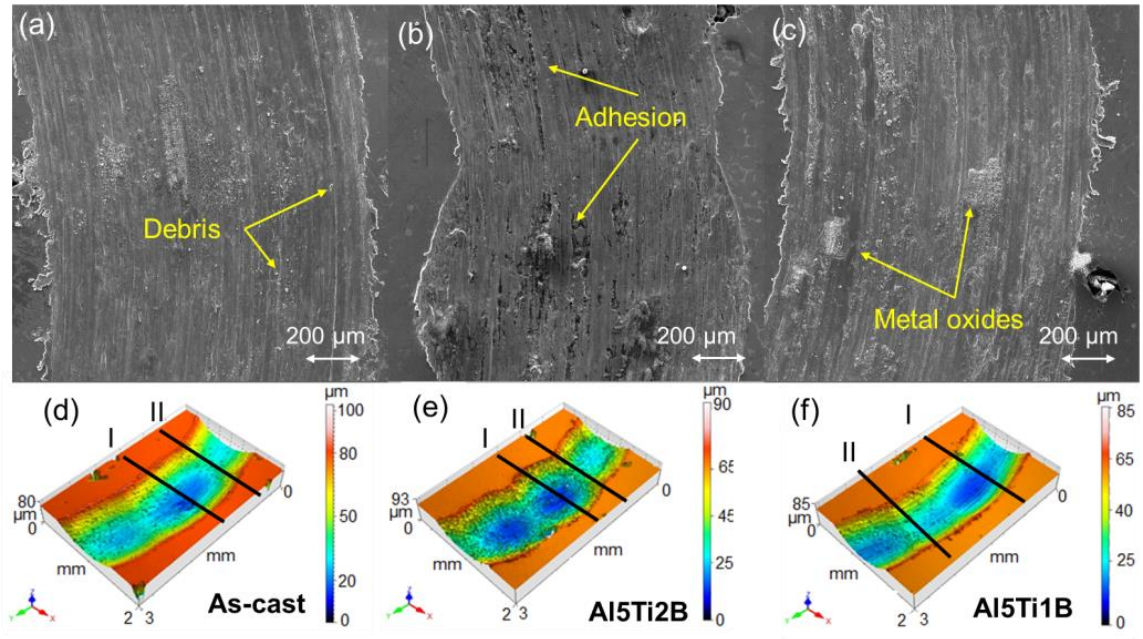

Figure 10. SEM images of wear track after the ball-on-disk testing from (**a**) as-cast; (**b**) Al5Ti2B; (**c**) Al5Ti2B 3D profiles obtained by OP images from (**d**) as-cast; (**e**) Al5Ti2B; (**f**) Al5Ti2B showing the spots of deep [I] and shallow regions [II] take in wear track from the 2D profile.

The wear track images showed in Figure 10a allow visualizing some debris accumulated during the testing by accumulation of aggregate aluminum particles in the sphere counterpart, which are detached during the test.

Wear surfaces in Figure 10a–c show the wear grooves, with some plastic deformation and delamination characteristics. The samples with Al5Ti2B grain refiner, observed in Figure 10b,e showed a different behavior with several subsequent circular deep shapes. Other samples showed worn tracks with some furrows typical of the abrasive-type wear mechanism visualized in Figure 10f. Adhesion and metal oxides are evident in Figure 10b,c. It seems that adhesion and delamination are the dominant mechanisms, preferentially in the Al5Ti2B condition.

From the 3D profiles obtained by OP shown in Figure 10d–f, deeper and shallow formations can be seen in all conditions. This situation is observed in the 2D surface profile in deep regions in Figure 11a and shallow regions (b) from respective localizations (I) and (II) in Figure 10d–f. The as-cast samples without grain refiner showed a deeper and wider worn track in both situations of samples wear track morphologies, with an average higher friction coefficient (µ) among all samples (Figure 12). Average friction coefficient (µ) was measured as an average of the values. The data were directly obtained from the test equipment. Although the condition with Al5Ti2B showed changed wear track morphology, the surface profile is very similar with the samplesAl5Ti2B (Figure 11).

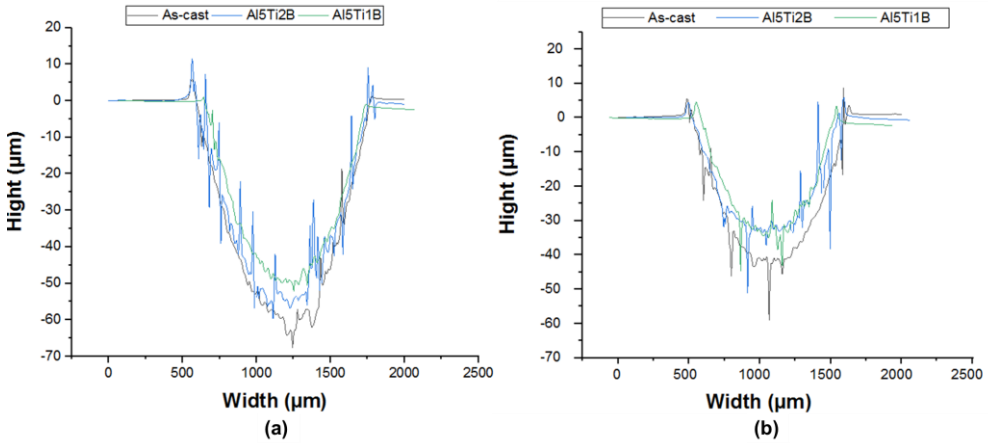

Figure 11. Comparison of 2D surface profile of A332 samples after wear test in (**a**) deep regions; (**b**) shallow of the wear tracks.

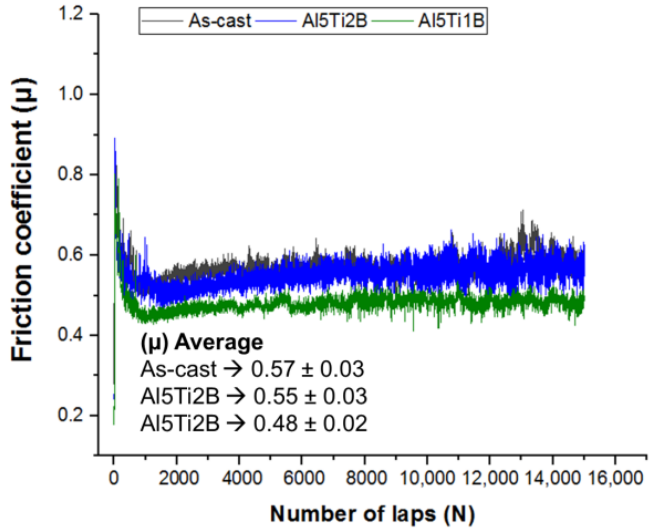

Figure 12. Friction coefficient in the ball-on-disk testing.

The 3D profilometry analysis allowed calculating of the wear volume loss in each sample. With volumetric wear losses, relative wear resistance (Ψ_h) was calculated in accordance with Equation (2). The results are shown in Table 4.

Table 4. Relative wear resistance.

Sample Material	As-Cast	Al5Ti2B	Al5Ti1B
Relative wear resistance	1	1.359	1.353

As-cast samples have the value of $\Psi_h = 1$ as they are from the same material, thus the reason is equal to one. The value was calculated from the volumetric loss standard W_{hE}, by the volumetric loss of the reference sample W_{hPV}. It is safe to assume that the volumetric loss of material reduces the wear resistance increase. Therefore, the values prove to be very close and there is no reason to believe any value is higher than other. Nevertheless, both results from the grain refiner's area are better than those of the as-cast condition.

In order to better understand the wear behavior of the alloy, as explained by Murray et al. [31], the relationship between wear conditions, hardness, and elastic modulus determined by nanoindentation was studied.

The relationship is designated by $\frac{H^3}{E_r^2}$, where H is hardness and E_r is the reduced elastic modulus and is known to be inversely proportional to wear [32–34]. The E_r is given by Equation (4):

$$\frac{1}{E_r} = \frac{E}{1-\nu^2} + \frac{E_i}{1-\nu_i^2} \quad (4)$$

where E e ν are, respectively, the measured material's modulus of elasticity and its Poisson's ratio; E_i and ν_i are the material's modulus of elasticity and Poisson's ratio of the tip material used in the indentation (in this case diamond). Figure 8a,b shows the hardness and elastic modulus respectively. In both cases, Fe-based intermetallic phases ($Al_{15}(FeMn)_3Si_2$; Al_5FeSi) show higher values than the primary aluminum matrix.

To determine the correlation between mechanical properties and wear, $\frac{H^3}{E_r^2}$ the index was calculated, which can be used to measure the elastic work. Generally, it is expected that higher values of $\frac{H^3}{E_r^2}$ indicate higher wear resistance [33].

In this way, by using instrumented nanoindentation with a matrix of 20 × 20, the map of the relationship $\frac{H^3}{E_r^2}$ was obtained, which is shown in Figure 13. Considering that this relationship is inversely proportional to wear (Equation (5)).

$$\frac{H^3}{E_r^2} \propto \frac{1}{\text{Material Wear}} \quad (5)$$

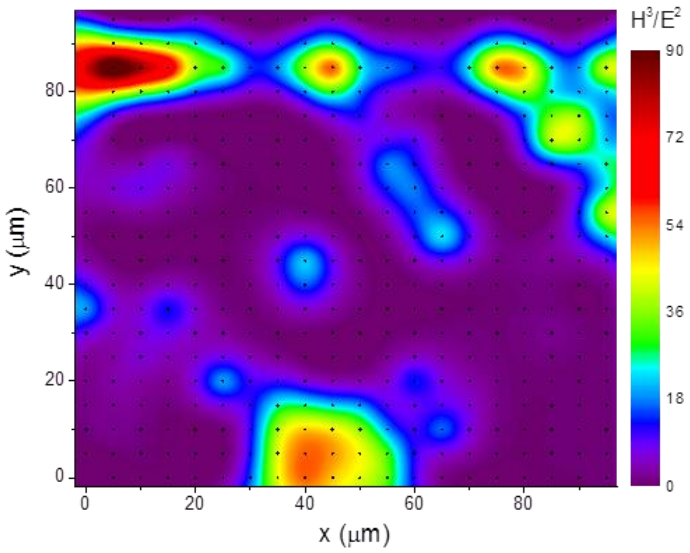

Figure 13. Map made using instrumented nanoindentation with a matrix of 20 × 20 indentations, made with respect to $\frac{H^3}{E_r^2}$.

It can be observed that the Fe-based intermetallic phase shows the higher index values, therefore, in the alloy with Al5Ti1B grain refiner, there is more and longer Al_5FeSi, matching with the lower volumetric wear loss in this condition. In addition, the friction coefficient results shown in Figure 12 are in accordance with these conclusions. Similar results were obtained with the Al5Ti2B grain refiner.

Therefore, it is possible to assert that when increasing the number of phases that satisfy a higher relation $\frac{H^3}{E_r^2}$ the wear of the part tends to decrease. Thus, there is a decrease in wear as the map colors tend to lean toward red and increase as they move towards blue (Figure 13). It can be seen that the Fe-based phase shows the highest values, which could be analyzed together with wear results and Al_5FeSi percentage in the alloy. These

results, apparently show that there is a link between the higher relation $\frac{H^3}{E_r^2}$, hardness and percentage of Al_5FeSi phase with the increase in wear resistance.

Finally, it can be asserted that the use of grain refiners (Al5Ti1B and Al5Ti2B) caused a refinement and an increase in the length of the intermetallic particles of Al_5FeSi, improving the wear resistance of the aluminum alloy A332.

3.5. Corrosion Analysis

Figure 14 shows the open circuit potential. All samples have shown a similar behavior regarding the open circuit potential. The average E_{ocp} calculated for the last 5 min of the measurement is shown in Table 5. A steady measurement means a steady state corrosion process, which is desired prior to any further analysis. It can be seen a slight tendency to reduce the values of open circuit potential (V) in the Al5Ti1B through time, an almost stable condition with small variations in the sample with Al5Ti2B refiner and a more significant variation in the as-cast sample.

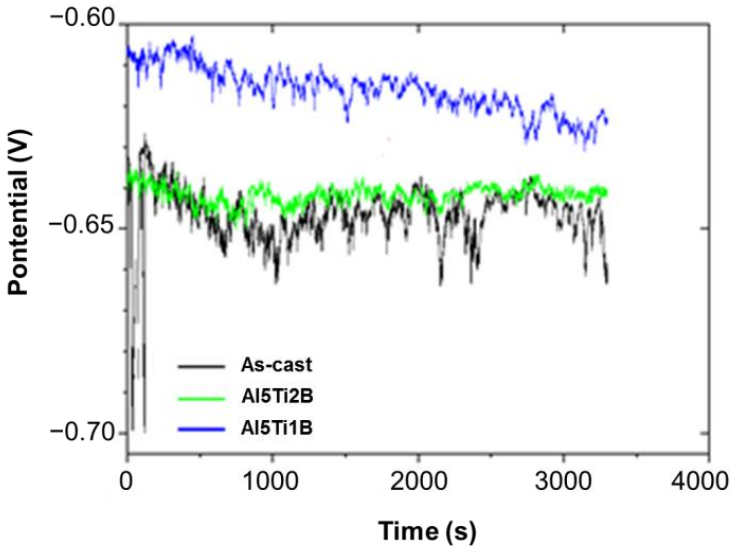

Figure 14. Open circuit potential from as-cast condition without grain refiner; grain refiner Al5Ti2B; grain refiner Al5Ti1B.

Table 5. Corrosion results for different conditions.

Sample	Rp (Ω)	Ba	Bc	Icorr ($\mu A/cm^2$)	Ecor (V)	Eocp (V)	η (V)	Corrosion Rate (mm/year)
As Cast	14,315	0.06434	1.2661	3.29	−0.7039	−0.6610	0.0429	0.034
Al5Ti2B	7305.6	0.05561	1.8894	12.1	−0.6015	−0.6408	−0.0393	0.126
Al5Ti1B	10,653	0.05926	0.8459	1.85	−0.6484	−0.6237	0.0247	0.019

Figure 15, shows Tafel plots for all the analyzed samples. The as-cast sample, which consists of A332 without refiner has shown, using ASTM G102 [24], a better corrosion resistance when compared to sample Al5Ti2B. Table 5 shows that the refiner used decreases corrosion resistance for Al5Ti2B. However, the open circuit potential and corrosion potential were slightly improved in samples refined with Al5Ti2B. Nevertheless, the current density increased, making it less resistant. Despite of the increase in the current density, pitting formation was observed at higher corrosion potential for both grain refiners. The refiner Al5Ti1B has preserved most of the corrosion resistance of the aluminum alloy while increasing pitting corrosion resistance.

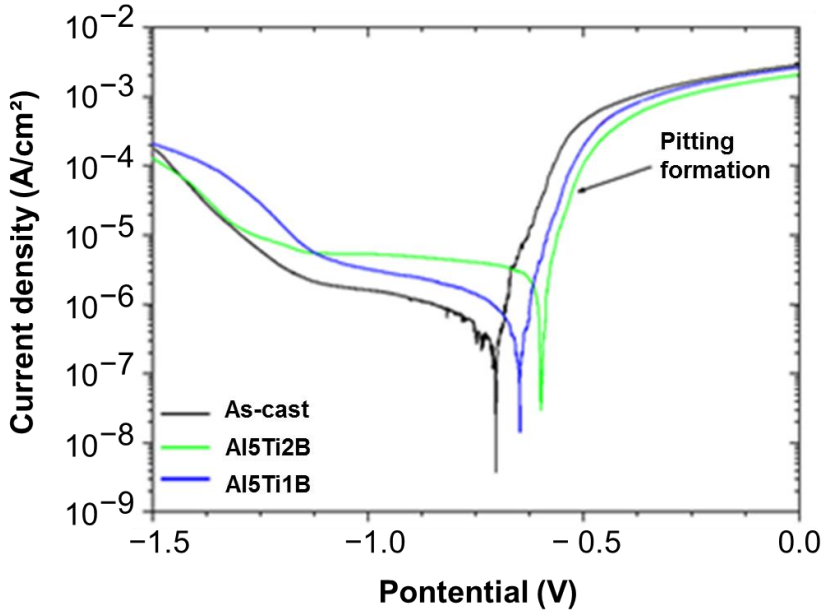

Figure 15. Tafel plots for the analyzed samples from as-cast condition without grain refiner; grain refiner Al5Ti2B; grain refiner Al5Ti1B.

In Figure 16, it is possible to see how the pitting grows across the materials. The Al_5FeSi phase works as an anodic site in corrosion reaction. For all the tested samples, it is possible to observe that the pitting either has to grow along the needles or to dodge it. For Al5Ti2B, it is possible to observe that pits are closer, which causes the anodic region created by them to overlap, which could be the reason of improvement in circuit potential and corrosion potential. Visually, Al5Ti1B has not drastically changed when compared to Al5Ti2B; however, an improvement is shown in the electrochemical corrosion. In the case of the as-cast, the observed pits were more superficial, even the pitting formation starting at lower values of corrosion potential.

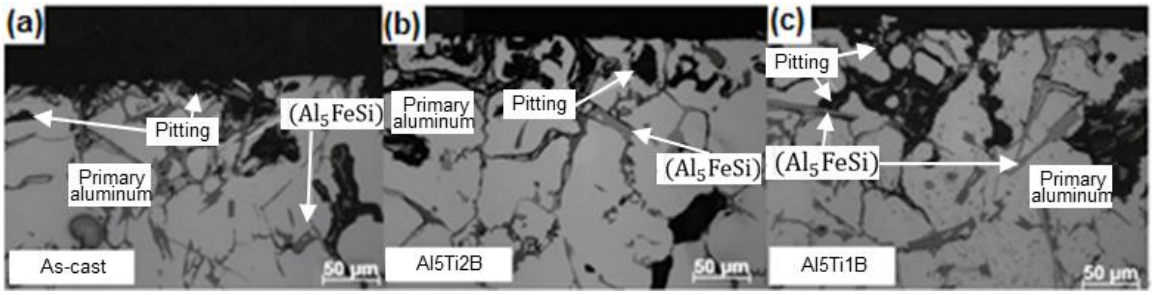

Figure 16. Optical micrographs of cross-section from (**a**) as-cast condition without grain refiner; (**b**) grain refiner Al5Ti2B; (**c**) grain refiner Al5Ti1B 500×.

4. Discussion

4.1. Microstructure Characterization

From OM and SEM images, the EDS analyses both alloys with and without different grain refiners presented the phases of primary aluminum, $Al_{15}(FeMn)_3Si_2$, Al_5FeSi, and Al_2Cu. The use of Sr modifier and grain refiners (Al5Ti2B and Al5Ti1B) promoted microstructural changes in the samples.

Cu-based intermetallic phases are commonly obtained in the Al-Si alloys. Moreover, the existence of this phase is well observed in the work Rakhmonov et al. [6], where the Al_2Cu phase appeared as a predominant Cu-rich one within the microstructure, in comparison with other small phases with Cu.

The Al_5FeSi intermetallic phase is not desirable in aluminum alloys, as it increases the material's brittleness. This is commonly found in the A332 aluminum alloy, as confirmed by Timelli et al. [26], who also reported this phase, characterized as Fe-bearing particles present in the microstructure, mainly in the form of Al_5FeSi in the form of needles, even if some particles in the form of $Al_{15}(FeMn)_3Si_2$ (Chinese-script) were detected.

In the A332 alloy, the dimensions of the Al_5FeSi intermetallic phase needles are influenced by the addition of Sr, as also concluded by Taghiabadi, et al. [35]. These authors observed that Sr, besides being effective in modifying eutectic silicon, also reduces the size of needle-shaped Al_5FeSi intermetallic compounds.

In addition, different thicknesses and sizes of needles were observed and this geometry has a relationship with the zone of the microstructure where they appear. In this sense, it can be seen that the thinner Al_5FeSi intermetallic were in the eutectic region and the thickest ones in the inside of the primary aluminum phase. These thicker intermetallic Al_5FeSi phase, probably served as nucleation sites of primary aluminum denoting its proeutectoid nature in these phases, as explained by Suarez-Peña and Asensio-Lozano [29]. The authors also comment that during the growth of primary aluminum dendrites, Fe is rejected in the residual liquid and the formation of the Al_5FeSi phase occurs in the eutectic phase controlled by the higher nucleation rate and lower growth compared to the Al_5FeSi intermetallic that form in the primary aluminum phase. As a result, this fraction of Al_5FeSi intermetallic formed at low temperatures is finer, as shown in the SEM images shown in Figure 5.

In spite of the dimensional changes of the Al_5FeSi phase, variations in the amounts of this intermetallic phase were not proven as a function of the type of refiner used, as found by El-Sayed [27]. This author also explains that the entry of hydrogen, which causes submerged oxide films, is the cause of hydrogen porosity and acts as a nucleation site for Fe-rich intermetallic. This Al_5FeSi phase nucleation phenomenon, which favors the proeutectoid formation of the phase, was not the main mechanism proven in the alloy processing conditions used in this work, where the intermetallic phase formed in the form of fine needles is mainly observed in the eutectic phase.

4.2. Primary Aluminum Phase Grain Size and Hardness

From the grain size and hardness analysis, the use of the Al5Ti2B refiner showed the worst results compared to the Al5Ti1B. This may be associated with a higher boron concentration, due to the likely agglomeration of TiB_2 particles, which is one of the biggest challenges of the refining process. With the increase in the fraction of B, it possibly caused an increase in the size of the bunches, impairing their efficiency in reducing the grain size [36]. The work by Xiao et al. [37], shows that the insertion of B in values higher than 0.03 wt.% reduces the refining capacity, which is attributed to the reaction of boron with Al_3Ti in a layer of TiB_2 and the consumption of solute Ti. Along with the above 0.03 wt.%, there is a gradual increase in refining performance, which is related to the formation of primary AlB_2 particles that provide additional nucleating substrates. However, as observed in this work, a greater amount of B well above to 2 wt.%, can possibly cause an agglomeration effect, which may impair its performance in grain refining.

Another significant aspect to consider is that in Al alloys with Si content above 4 wt.%, there is a reduction in the performance of grain reduction of the refined alloys [38]. The Ti present in the refiner alloys reacts with Si to form titanium silicates that decrease the Ti content in the molten bath, thus reducing the efficiency of grain refinement [39].

In addition, the use of refiners (AlTiB), caused an increase in the size and a decrease in the thickness of the needles of the Al_5FeSi phase, as demonstrated in the analysis in Figure 6. This phenomenon also influences the increase in microhardness, as observed by Samuel et al. [7], who explained that the needles of the Al_5FeSi present in the microstructures of alloy A332 may be responsible for an increase in the brittleness and hardness of the alloy.

4.3. Effect of Grain Refiner Addition on Wear Behavior

After the ball-on-disk test, it could be seen that some debris accumulated in the sample without grain refiner (Figure 10a). These particles probably accumulated in some parts promoting the formation of deeper structures before, where the material was taken from. This mechanism was also visualized and explained by Pukasiewicz et al. [40], who also noted that a smaller amount of debris observed, may reduce the friction coefficient.

Alipour et al. [41], when analyzing the effect of Al–8B grain refiner and heat treatment conditions in the wear of Al–12Zn–3Mg–2.5Cu aluminum alloys, observed similar results with delamination and adhesion mechanisms. The authors assert that delamination wear is the dominant mechanism in the early stages of sliding, probably due to the microstructural formation. The presence of metal oxides on the surface is also characteristic of this process. Alipour et al. [42] observed similar results when studying the effect of Al5Ti1B grain refiner on the dry sliding wear behavior of an Al–Zn–Mg–Cu alloy. The authors show that regions with a detached layer in the form of craters or cavities could indicate locally adhesive wear, probably because of the formation and breaking of micro-welds during sliding.

Thus, overall worn-surface study reveals that the A332 alloys tend to exhibit three types of wear mechanisms such as adhesive, abrasive, and oxidative wear. Abrasive wear was mainly observed in the case of as-cast alloy without refiners. Adhesive and oxidative types of wear were mostly observed in the case of the alloy containing grain refiner [43].

The analysis of wear resistance material showed lower values in the as-cast samples without grain refiners compared to samples with grain refiners (Al5Ti1B or Al5Ti2B). This behavior occurs despite the lower friction coefficient ($\mu = 0.48$) observed in samples refined with Al5Ti1B. This previous behavior is related to the incidence of microstructural refinement and Al_5FeSi phase and hardness in the wear mechanisms of the refined A332 alloy. It was proved that the microstructural refinement led to an improvement in wear resistance according to Archard's Law of Wear, that is, the increase in hardness obtained by grain refinement, provided a increase in material wear resistance [43].

In addition, the smallest grain size from Al5Ti2B also relate to the higher wear resistance, although the values are very close to Al5Ti1B. Prasada Rao et al. [44], after analyzing commercially pure Al grain refined using Al–Ti and Al–Ti–B grain refiner master alloys in the wear test, found similar results. The authors commented that wear rates decreased with a decrease in grain size, probably due to grain shape transformed from columnar to equiaxed. In their work, the grain size differences were more distinct, which could lead to these observed results.

However, other microstructural factors such as the presence of Al_5FeSi intermetallic phases, as well as volume fraction, thickness, and size, can influence the wear resistance of the alloy. In this sense, Abouei et al. [45] found that similar needle intermetallic phases decreased the wear resistance in Al-Si alloys, due to the higher tendency to form micro-cracking.

Summarizing the findings, using grain refiners (5Ti1B and Al5Ti2B) helped improve the wear resistance of the A332 cast samples. The modifications in intermetallic phases may be the main cause for the observed wear resistance increase.

4.4. Corrosion Analysis

For the A332 alloy tested in this case, the phases may cause changes in isolated characteristics, resulting in global modifications. Such is the case of phase Al_5FeSi, which can act as a cathodic function for corrosion. As mentioned by Orlowska et al. [46], in aluminum alloys, the pitting and initial corrosion are generally related to intermetallic phases. A majority of them have Fe (Al_3Fe, AlFeSi) present in the alloy, which is more cathodic to matrix primary aluminum. Therefore, in these cases the adjacent matrix primary aluminum dissolves around them. The pit propagation in proximity of Fe-phase is one of the corrosion mechanisms observed [35]. According to Ralston and Birbilis, [18], the grain refining process itself may disrupt local chemical microstructure through second phases and thus the chemical and ensuing electrochemical heterogeneity of the material.

The Al_5FeSi phase, at some point meets the grain boundaries, as shown in Figure 16, supporting the intergranular corrosion in direction to primary aluminum. This mechanism is as abundantly found in the literature. Ahmed et al. [47] analyzed this effect in Al-2.5% Mg cast alloy, which was modified by adding 0.5 Ti and 0.1 B wt.%. Their results showed intergranular corrosion that started in tiny pits and continued to expand across the grain boundaries. The refined alloy exhibited improved corrosion resistance owing to the refined and minimized grain structure.

According to the microstructural analysis mentioned above, the eutectic phase present more lamellar in the alloys with grain refiner due to the effect of the Sr. Therefore, in comparison with acicular-shaped formations of the as-cast conditions, modified alloys present lamellar formations which has more area and more galvanic couplings may occur, due to the fact that it acts as a local cathode to primary aluminum, by dissolving it [48]. Similar results were observed by Ma et al. [49] when the microstructures and corrosion resistances of hypoeutectic Al-6.5Si-0.45 Mg casting alloys with the addition of both Sc and Zr were researched. Corrosion tests were made in 3.5 wt.% NaCl with an increase in exposure time. The author comments that the tested alloys with fine eutectic Si exhibit poorer corrosion resistance than those with coarse eutectic and dissolving primary aluminum phase. They attribute these findings to the galvanic couplings which can be formed between the eutectic (as a cathode) and primary aluminum (as an anode). More galvanic couplings can be formed in the test alloys with a fine eutectic.

There is no consensus about the corrosion rate of alloys with and without a grain refiner. However, Ozturk et al. [50] achieved a dramatically improved corrosion resistance with grain refiners. They evaluated the corrosion behavior of A356 aluminum alloy refined with Al5Ti1B and Al3B and modified with Sr. Electrochemical measurements were realized in 3.5 wt.% NaCl solution. The authors show a clear improvement in the corrosion resistance compared to the unmodified A356 alloy in the sequence as follows: 170 ppm Sr-modified alloy, B grain-refined, and Ti-B grain-refined A356. The main reason is associated with microstructural formation, with different situations for B and Ti. The authors explain that for B grain-refined alloy, the whole surface of the corroded region seems to be dissolved; in contrast, in Ti grain-refined castings, local dendrites remain present with eutectic regions that were dissolved. Therefore, based on this, higher amounts of B in the grain refiner Al5Ti2B probably mean significant corrosion to as-cast and Al5Ti1B grain refiner. Overall, based on the revised literature, and the review of Wang et al. [9], there is a lack of consensus on how grain refinement affects the corrosion behavior of materials. Both the improvement and deterioration of corrosion resistance have been observed with grain refinement.

5. Conclusions

A comparison between two grain refiners (Al5Ti2B and Al5Ti1B) shows that their use promoted an effective grain size reduction. Corrosion analyses show some mechanisms related with phase interactions, furthermore, the elastic modulus of the phases helps to understand their influence in the hardness and corrosion mechanisms. The following conclusions were drawn from this work:

- Effective dispersion of grain refinement was achieved when using the melting temperature of 750 °C. The procedure adopted can be used to insert the Al5Ti1B and Al5Ti2B master alloys in the A332 alloy with an induction furnace.
- The morphology of elongated arms of dendrites of primary aluminum changes to more equiaxed grains when the grain refiners (Al5Ti1B or Al5Ti2B) are added. This modification of the shape and size of the grains results from increasing the formation of solidification nuclei through different refining utilized. Furthermore, the image analysis allowed a note of the modifications from acicular-shaped to lamellar due to the presence of the Sr modifier.
- The fundamental function of the grain refiner was successfully obtained using both master alloys. The grain refiners (Al5Ti2B and Al5Ti1B) are adequate to achieve smaller grain sizes for the A332 aluminum alloy compared to as-cast conditions,

probably promoting adequate places for heterogeneous nucleation. Al5Ti1B was the most effective grain refiner, reducing (33.3 ± 3.3 μm) in comparison with Al5Ti2B (38.8 ± 4.4 μm).

- The average hardness increased after adding grain refiner due to the Hall–Petch relation and Fe-based intermetallic phase length increases. Albeit the non-homogeneous grain size through the samples led to a significant variation in the values of the standard deviation factor. Hence, it is not possible to confirm if there is any improvement in microhardness with the addition of different refiners.
- In the combined addition of grain refiner and modifier samples, Fe-based intermetallic phase Al_5FeSi measurements indicate an increase in the phase length. The Al5Ti2B condition presents volumetric fraction values (4.2 ± 0.74%) slightly higher than the other (Al5Ti1B), around 3.6 ± 1,45%. This higher fraction of Al_5FeSi could be responsible for the slight difference in the wear resistance. The data index $\frac{H^3}{E_r^2}$ obtained from the nanoindentation analysis shows a relation with the higher resistance to the wear of the Al_5FeSi phase.
- Addition of grain refiners improved the relative wear resistance. Although the difference between them is modest because the values are 1.359 to Al5Ti2B and 1.353 to Al5Ti1B, both values are higher to those of the as-cast condition (1), used as a reference. The observed effect might be linked to a refinement and an increase in the length of the intermetallic particles Al_5FeSi, which would be related to the improved wear resistance of the aluminum alloy A332.
- A relation between corrosion resistance and addition of grain refiner cannot be established. While Al5Ti2B has shown an overall decrease in corrosion resistance, Al5Ti1B has an enhanced performance. Nonetheless, pitting morphology should be considered before the use of grain refinement. Although the pitting formation started at a higher corrosion potential with the use of grain refiners, the optical microscopy images have shown deeper pits. Furthermore, the Al_5FeSi phase acts as a cathodic function in the corrosion reaction, dissolving the adjacent matrix, primary aluminum, and generating pit growth.

Author Contributions: Conceptualization, H.D.C.F., B.E.A. and L.A.L.; methodology, B.E.A., A.R.M., W.R.d.O., L.A.L. and H.D.C.F.; validation, W.R.d.O., A.R.M., E.M.-C. and H.D.C.F.; formal analysis, W.R.d.O., A.R.M., B.E.A.; investigation, B.E.A., H.D.C.F., A.R.M. and W.R.d.O.; resources, H.D.C.F., E.M.-C. and L.A.L.; data curation, H.D.C.F. and L.A.L.; writing—original draft preparation, B.E.A. and H.D.C.F.; writing—review and editing, A.R.M., W.R.d.O. and A.G.M.P.; visualization, E.M.-C.; supervision, H.D.C.F., A.G.M.P., E.M.-C. and L.A.L.; project administration, L.A.L. and H.D.C.F. All authors have read and agreed to the published version of the manuscript.

Funding: This research was funded by Coordination for the Improvement of Higher Education Personnel—Brazil (CAPES)—Financing Code 001, providing a master's degree scholarship.

Institutional Review Board Statement: Not applicable.

Informed Consent Statement: Not applicable.

Data Availability Statement: The raw data and data required to reproduce these findings are available for download from [51].

Acknowledgments: The authors would like to thank the Graduate Program (DIRPPG) from the Technological Federal University of Paraná (UTFPR), The National Council for Scientific and Technological Development (CNPq)/Araucaria Foundation for aid in promotion, and The Centro de Caracterização Multiusuário em Pesquisa e Desenvolvimento de Materiais (C2MMa) for the analyses conducted.

Conflicts of Interest: The authors declare no conflict of interest.

References

1. Zhang, H.; Chen, G.; Zhang, Z.; Zhao, Y.; Mu, S.; Xu, J.; Zhang, T. Study on the Grain Refinement of A356 Alloy by Al–3 Wt-% VN Master Alloy. *Mater. Sci. Technol.* **2020**, *36*, 819–826. [CrossRef]
2. Zhu, M.; Jian, Z.; Yang, G.; Zhou, Y. Effects of T6 Heat Treatment on the Microstructure, Tensile Properties, and Fracture Behavior of the Modified A356 Alloys. *Mater. Des.* **2012**, *36*, 243–249. [CrossRef]
3. Nogita, K.; Dahle, A.K. Effects of Boron on Eutectic Modification of Hypoeutectic Al–Si Alloys. *Scr. Mater.* **2003**, *48*, 307–313. [CrossRef]
4. Yan, W.; Fu, G.; Xu, Y.; Lai, W.; Chen, H. Effect of Sr Addition on the Microstructure and Properties of the A356 Al Alloy. *Mater. Tehnol.* **2021**, *55*, 443–448. [CrossRef]
5. Prema, S.; Chandrashekharaiah, T.M.; Farida Begum, P. Effect of Grain Refiners and/or Modifiers on the Microstructure and Mechanical Properties of Al-Si Alloy (Lm6). *Mater. Sci. Forum* **2019**, *969*, 794–799. [CrossRef]
6. Rakhmonov, J.; Timelli, G.; Bonollo, F. Influence of Melt Superheat, Sr Modifier, and Al-5Ti-1B Grain Refiner on Microstructural Evolution of Secondary Al-Si-Cu Alloys. *Metall. Mater. Trans. A* **2016**, *47*, 5510–5521. [CrossRef]
7. Samuel, E.; Golbahar, B.; Samuel, A.M.; Doty, H.W.; Valtierra, S.; Samuel, F.H. Effect of Grain Refiner on the Tensile and Impact Properties of Al–Si–Mg Cast Alloys. *Mater. Des.* **2014**, *56*, 468–479. [CrossRef]
8. Wyrzykowski, J.W.; Grabski, M.W. The Hall–Petch Relation in Aluminium and Its Dependence on the Grain Boundary Structure. *Philos. Mag. A* **1986**, *53*, 505–520. [CrossRef]
9. Wang, P.-J.; Ma, L.-W.; Cheng, X.-Q.; Li, X.-G. Influence of Grain Refinement on the Corrosion Behavior of Metallic Materials: A Review. *Int. J. Miner. Metall. Mater.* **2021**, *28*, 1112–1126. [CrossRef]
10. Moldovan, P.; Popescu, G. The Grain Refinement of 6063 Aluminum Using Al-5Ti-1B and Al-3Ti-0.15C Grain Refiners. *JOM* **2004**, *56*, 59–61. [CrossRef]
11. Vončina, M.; Medved, J.; Jerina, L.; Paulin, I.; Cvahte, P.; Steinacher, M. The Impact of Al-Ti-B Grain-Refiners from Different Manufacturers on Wrought Al-Alloy. *Arch. Metall. Mater.* **2019**, *64*, 739–746. [CrossRef]
12. Gyarmati, G.; Bogoly, L.; Stawarz, M.; Fegyverneki, G.; Kéri, Z.; Tokár, M.; Mende, T. Grain Refiner Settling and Its Effect on the Melt Quality of Aluminum Casting Alloys. *Materials* **2022**, *15*, 7679. [CrossRef] [PubMed]
13. Limmaneevichitr, C.; Eidhed, W. Fading Mechanism of Grain Refinement of Aluminum–Silicon Alloy with Al–Ti–B Grain Refiners. *Mater. Sci. Eng. A* **2003**, *349*, 197–206. [CrossRef]
14. Choudhary, C.; Sahoo, K.L.; Roy, H.; Mandal, D. Effect of Grain Refiner on Microstructural Feature Influence Hardness and Tensile Properties of Al-7Si Alloy. *J. Mater. Eng. Perform.* **2022**, *31*, 3262–3273. [CrossRef]
15. Tunçay, T. The Effect of Modification and Grain Refining on the Microstructure and Mechanical Properties of A356 Alloy. *Acta Phys. Pol. A* **2017**, *131*, 89–91. [CrossRef]
16. Çolak, M.; Arslan, İ. Investigation of the Effect of the Addition of Grain Refiner and Modifier Addition on Wear Properties in Sand and Permanent Mould Casting of A357 and A380 Aluminium Alloys. *Int. J. Cast Met. Res.* **2022**, *35*, 17–23. [CrossRef]
17. Sumalatha, C.; Rao, P.V.C.S.; Rao, V.V.S.; Deepak, M.S.K. Influence of Grain Refiner, Modifier and Graphene on the Dry Sliding Wear of Hypereutectic Al–Si Alloys. *Metallogr. Microstruct. Anal.* **2022**, *11*, 234–244. [CrossRef]
18. Ralston, K.D.; Birbilis, N. Effect of Grain Size on Corrosion: A Review. *Corrosion* **2010**, *66*, 75005–75013. [CrossRef]
19. Abd El-Aziz, K.; Ahmed, E.M.; Alghtani, A.H.; Felemban, B.F.; Ali, H.T.; Megahed, M.; Saber, D. Development of Al-Mg-Si Alloy Performance by Addition of Grain Refiner Al-5Ti-1B Alloy. *Artic. Sci. Prog. Sci. Prog.* **2021**, *104*, 1–15. [CrossRef]
20. Guan, R.-G.G.; Tie, D. A Review on Grain Refinement of Aluminum Alloys: Progresses, Challenges and Prospects. *Acta Metall. Sin.* **2017**, *30*, 409–432. [CrossRef]
21. *ASTM E112*; StandardTest Methods for Determining Average Grain Size. ASTM: West Conshohocken, PA, USA, 2013.
22. Vargova, M.; Tavodova, M.; Monkova, K.; Dzupon, M. Research of Resistance of Selected Materials to Abrasive Wear to Increase the Ploughshare Lifetime. *Metals* **2022**, *12*, 940. [CrossRef]
23. *ASTM G59*; Standard Test Method for Conducting Potentiodynamic Polarization Resistance Measurements. ASTM: West Conshohocken, PA, USA, 2009.
24. *ASTM G102*; Standard Practice for Calculation of Corrosion Rates and Related Information from Electrochemical Measurements. ASTM: West Conshohocken, PA, USA, 1989.
25. *ASTM G5*; Standard Reference Test Method for Making Potentiodynamic Anodic Polarization Measurements. ASTM: West Conshohocken, PA, USA, 2004.
26. Timelli, G.; Caliari, D.; Rakhmonov, J. Influence of Process Parameters and Sr Addition on the Microstructure and Casting Defects of LPDC A356 Alloy for Engine Blocks. *J. Mater. Sci. Technol.* **2016**, *32*, 515–523. [CrossRef]
27. El-Sayed, M.A. The Behaviour of Bifilm Defects in Cast Al-7Si-Mg Alloy. *PLoS ONE* **2016**, *11*, e0160633. [CrossRef] [PubMed]
28. Dinnis, C.M.; Taylor, J.A.; Dahle, A.K. As-Cast Morphology of Iron-Intermetallics in Al-Si Foundry Alloys. *Scr. Mater.* **2005**, *53*, 955–958. [CrossRef]
29. Suárez-Peña, B.; Asensio-Lozano, J. Influence of Sr Modification and Ti Grain Refinement on the Morphology of Fe-Rich Precipitates in Eutectic Al-Si Die Cast Alloys. *Scr. Mater.* **2006**, *54*, 1543–1548. [CrossRef]
30. Gencalp Irizalp, S.; Saklakoglu, N. Effect of Fe-Rich Intermetallics on the Microstructure and Mechanical Properties of Thixoformed A380 Aluminum Alloy. *Eng. Sci. Technol. Int. J.* **2014**, *17*, 58–62. [CrossRef]

31. Murray, J.W.; Ahmed, N.; Yuzawa, T.; Nakagawa, T.; Sarugaku, S.; Saito, D.; Clare, A.T. Dry-Sliding Wear and Hardness of Thick Electrical Discharge Coatings and Laser Clads. *Tribol. Int.* **2020**, *150*, 106392. [CrossRef]
32. Wang, Q.; Luo, S.; Wang, S.; Wang, H.; Ramachandran, C.S. Wear, Erosion and Corrosion Resistance of HVOF-Sprayed WC and Cr3C2 Based Coatings for Electrolytic Hard Chrome Replacement. *Int. J. Refract. Met. Hard Mater.* **2019**, *81*, 242–252. [CrossRef]
33. Szala, M.; Walczak, M.; Pasierbiewicz, K.; Kamiński, M. Cavitation Erosion and Sliding Wear Mechanisms of AlTiN and TiAlN Films Deposited on Stainless Steel Substrate. *Coatings* **2019**, *9*, 340. [CrossRef]
34. Fals, H.C.; Lourençato, L.A.; Orozco, M.S.; Belém, M.J.X.; Lima, C.R.C. Slurry Erosion Resistance of Thermally Sprayed Nb2O5 and Nb2O5+WC12Co Composite Coatings Deposited on AISI 1020 Carbon Steel. *Ceram. Int.* **2020**, *46*, 27670–27678. [CrossRef]
35. Taghiabadi, R.; Ghasemi, H.M.; Shabestari, S.G. Effect of Iron-Rich Intermetallics on the Sliding Wear Behavior of Al-Si Alloys. *Mater. Sci. Eng. A* **2008**, *490*, 162–170. [CrossRef]
36. Alamdari, H.D.; Dubé, D.; Tessier, P. Behavior of Boron in Molten Aluminum and Its Grain Refinement Mechanism. *Metall. Mater. Trans. A Phys. Metall. Mater. Sci.* **2013**, *44*, 388–394. [CrossRef]
37. Xiao, F.; Wu, M.-X.; Wang, Y.-X.; Zhou, W.-Z.; Wang, S.-B.; Wang, D.-H.; Zhu, G.-L.; Jiang, M.; Shu, D.; Mi, J.-W.; et al. Effect of Trace Boron on Grain Refinement of Commercially Pure Aluminum by Al–5Ti–1B. *Trans. Nonferrous Met. Soc. China* **2022**, *32*, 1061–1069. [CrossRef]
38. Johnsson, M. Influence of Si and Fe on the Grain Refinement of Aluminium. *Int. J. Mater. Res.* **1994**, *85*, 781–785. [CrossRef]
39. Bolzoni, L.; Hari Babu, N. Efficacy of Borides in Grain Refining Al-Si Alloys. *Metall. Mater. Trans. A Phys. Metall. Mater. Sci.* **2019**, *50*, 746–756. [CrossRef]
40. Pukasiewicz, A.G.M.; de Oliveira, W.R.; Váz, R.F.; de Souza, G.B.; Serbena, F.C.; Dosta, S.; Cano, I.G. Influence of the Deposition Parameters on the Tribological Behavior of Cold Gas Sprayed FeMnCrSi Alloy Coatings. *Surf. Coat. Technol.* **2021**, *428*, 127888. [CrossRef]
41. Alipour, M.; Azarbarmas, M.; Heydari, F.; Hoghoughi, M.; Alidoost, M.; Emamy, M. The Effect of Al-8B Grain Refiner and Heat Treatment Conditions on the Microstructure, Mechanical Properties and Dry Sliding Wear Behavior of an Al-12Zn-3Mg-2.5Cu Aluminum Alloy. *Mater. Des.* **2012**, *38*, 64–73. [CrossRef]
42. Alipour, M.; Aghdam, B.G.; Rahnoma, H.E.; Emamy, M. Investigation of the Effect of Al-5Ti-1B Grain Refiner on Dry Sliding Wear Behavior of an Al-Zn-Mg-Cu Alloy Formed by Strain-Induced Melt Activation Process. *Mater. Des.* **2013**, *46*, 766–775. [CrossRef]
43. Zmitrowicz, A. Wear Patterns and Laws of Wear—A Review. *J. Theor. Appl. Mech.* **2006**, *44*, 219–253.
44. Prasada Rao, A.K.; Das, K.; Murty, B.S.; Chakraborty, M. Microstructure and the Wear Mechanism of Grain-Refined Aluminum during Dry Sliding against Steel Disc. *Wear* **2008**, *264*, 638–647. [CrossRef]
45. Abouei, V.; Saghafian, H.; Shabestari, S.G.; Zarghami, M. Effect of Fe-Rich Intermetallics on the Wear Behavior of Eutectic Al-Si Piston Alloy (LM13). *Mater. Des.* **2010**, *31*, 3518–3524. [CrossRef]
46. Orłowska, M.; Ura-Bińczyk, E.; Olejnik, L.; Lewandowska, M. The Effect of Grain Size and Grain Boundary Misorientation on the Corrosion Resistance of Commercially Pure Aluminium. *Corros. Sci.* **2019**, *148*, 57–70. [CrossRef]
47. Ahmed, H.M.; Ahmed, H.A.M.; Hefni, M.; Moustafa, E.B. Effect of Grain Refinement on the Dynamic, Mechanical Properties, and Corrosion Behaviour of Al-Mg Alloy. *Metals* **2021**, *11*, 1825. [CrossRef]
48. Arthanari, S.; Jang, J.C.; Shin, K.S. Corrosion Studies of High Pressure Die-Cast Al-Si-Ni and Al-Si-Ni-Cu Alloys. *J. Alloys Compd.* **2018**, *749*, 146–154. [CrossRef]
49. Ma, Y.; Liu, Y.; Wang, M. Microstructures and Corrosion Resistances of Hypoeutectic Al-6.5Si-0.45 Mg Casting Alloy with Addition of Sc and Zr. *Mater. Chem. Phys.* **2022**, *276*, 125321. [CrossRef]
50. Öztürk, İ.; Hapçı Ağaoğlu, G.; Erzi, E.; Dispinar, D.; Orhan, G. Corrosion Behavior of B and Ti Grain-Refined Sr-Modified A356. *J. Mater. Eng. Perform.* **2018**, *27*, 5197–5204. [CrossRef]
51. Arendarchuck, B.E. "Database 3", Mendeley Data, V2. 2022. Available online: https://data.mendeley.com/datasets/r7rj6bzs6j/2 (accessed on 12 December 2022).